

MITO: A Millimeter-Wave Dataset and Simulator for Non-Line-of-Sight Perception

Laura Dodds^{1,*}, Tara Boroushaki^{1,*}, Cusuh Ham², Fadel Adib^{1,3}

ldodds@mit.edu, tarab@mit.edu, ham@adobe.com, fadel@mit.edu

¹ Massachusetts Institute of Technology, ² Adobe Research, ³ Cartesian Systems

* These authors contributed equally

Abstract

The ability to observe the world is fundamental to reasoning and making informed decisions on how to interact with the environment. However, optical perception can often be disrupted due to common occurrences, such as occlusions, which can pose challenges to existing vision systems. We present MITO, the first millimeter-wave (mmWave) dataset of diverse, everyday objects, collected using a UR5 robotic arm with two mmWave radars operating at different frequencies and an RGB-D camera. Unlike visible light, mmWave signals can penetrate common occlusions (e.g., cardboard boxes, fabric, plastic) but each mmWave frame has much lower resolution than typical cameras. To capture higher-resolution mmWave images, we leverage the robot’s mobility and fuse frames over the synthesized aperture. MITO captures over 24 million mmWave frames and uses them to generate 550 high-resolution mmWave (synthetic aperture) images in line-of-sight and non-light-of-sight (NLOS), as well as RGB-D images, segmentation masks, and raw mmWave signals, taken from 76 different objects. We develop an open-source simulation tool that can be used to generate synthetic mmWave images for any 3D triangle mesh. Finally, we demonstrate the utility of our dataset and simulator for enabling broader NLOS perception by developing benchmarks for NLOS segmentation and classification.

1. Introduction

Recent decades have witnessed many impressive advancements in computer vision, with state-of-the-art systems capable of high-accuracy object detection, segmentation, classification, and more. One of the main applications of these advances is in robotic manipulation and perception, where autonomous robots are expected to find and retrieve objects and navigate through complex environments spanning warehouses, manufacturing plants, and smart homes.

However, relying primarily on optical perception (e.g., cameras, LiDARs, etc) inherently limits existing systems to line-of-sight (LOS).¹ For example, a camera-based system

¹While some visible-light systems can rely on reflected laser light to image objects around the corner, they cannot image fully occluded items (e.g., within a closed box).

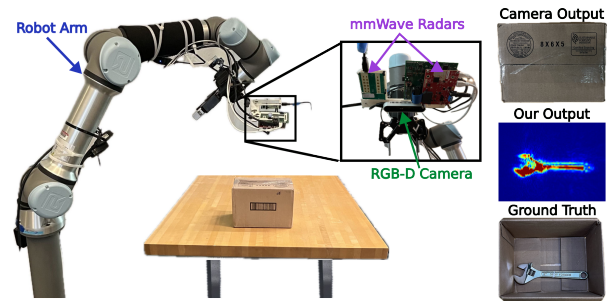


Figure 1. MITO. We use a robotic arm to move mmWave radars throughout the environment. While an RGB-D camera’s output cannot see inside the box, we produce high-resolution non-line-of-sight mmWave images.

cannot see inside a closed box to confirm e-commerce orders are correct or detect broken objects during shipping. Nor is it feasible for camera-based robots to efficiently plan complex, multi-step tasks in practical environments where required objects may be fully occluded.

Instead, it is possible to produce non-line-of-sight (NLOS) images using millimeter-wave (mmWave) radars [6]. Unlike visible light, mmWave wireless signals can traverse everyday occlusions such as cardboard, fabric, and plastic. This allows mmWave radars to image objects in non-line-of-sight, similar to how airport security scanners produce high-resolution NLOS images of passengers to detect hidden weapons. With the emergence of low-cost mmWave radars, it is possible to build pervasive autonomous systems with this NLOS imaging capability. For example, using mmWave radars attached to a robotic arm (Fig. 1), we can produce a NLOS mmWave image of a wrench within a closed box.

However, to achieve the many possible applications of NLOS imaging, we need to be able to *perceive* (e.g., segment, classify, etc) objects within these images. Unfortunately, these images are fundamentally different from visible-light images in multiple ways. First, they suffer from radar-specific artifacts; for example, the much longer wavelength of millimeter-waves versus visible light (hundreds of nanometers) results in fundamentally different specular and diffuse properties of imaged objects. Second, mmWave images have no color information. Third, they are complex-valued.² Therefore, since the majority of ex-

²Interestingly, the values are dependent on not only the location of the

isting perception algorithms have not been trained on these mmWave images, they need to be adapted for NLOS perception; in some cases, we may require entirely new algorithms or models to enable mmWave-based perception to approach the accuracy of visual-light-based perception (as we show in this paper).

Inspired by how early imaging datasets, such as MSRC [21], Pascal [19], Berkeley 3D [26], and YCB [14], paved the way for many advancements within computer vision, we believe that a dataset of mmWave images of everyday objects is fundamental for enabling pervasive NLOS perception. To summarize, we make the following key contributions:

- **Dataset.** We create MITO, a novel dataset of mmWave images for everyday objects, using a custom-built robotic imaging system and signal processing pipeline. We capture over 24 million mmWave frames, and use them to generate 550 images of 76 objects from the YCB dataset (out of a total of 80 objects) in both line-of-sight and non-line-of-sight. For each object, we capture mmWave images at multiple different frequencies. We also provide RGB-D images of the objects (when in LOS) and ground truth object segmentations.
- **Simulator.** We develop an open-source simulator that can produce synthetic mmWave images for any 3D triangle mesh. Since different materials interact differently with mmWave signals and, therefore, produce different images, we build two different modeling methods into our simulation, the combination of which can be used to simulate a wide range of material properties.
- **Non-line-of-sight Applications.** Using MITO, we establish baselines for two computer vision tasks in non-line-of-sight. First, we show object segmentation, using the segment-anything model (SAM) [27] and a mmWave power-based prompter. Second, we show shape classification, which is trained entirely on synthetic images and can classify real-world images.

The dataset, code, and a video demonstration are available here:

https://github.com/signalkinetics/MITO_Codebase

2. Related Work

mmWave Datasets. Recognizing the importance of millimeter-wave perception, past research has made initial steps towards millimeter-wave datasets. However, the vast majority of them are focused either on imaging humans [15, 16, 16, 37, 46, 48] for action recognition, outdoor imaging for autonomous driving [11, 13, 22, 23, 28, 34, 35, 45, 49, 51], or imaging of building interiors (walls, hallways) [12, 36]. In the context of higher resolution imaging of objects, the only dataset that we are aware of is fo-object, but also the material and texture.

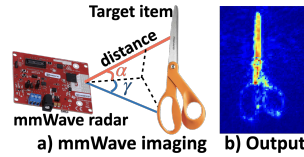


Figure 2. **mmWave Imaging** a) mmWave radars estimate range and angle-of-arrival to produce b) reflection maps.

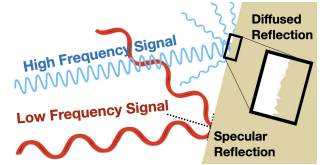


Figure 3. **Diffuse and Specular Reflections.** The frequency of a signal changes the type of reflections it experiences for the same surface.

cused on guns and knives for TSA and detecting concealed weapons through body scanners for airport security applications [31, 38, 39]. Our work, however, is focused on generating a dataset of a larger, diverse set of everyday objects for application such as robotic manipulation and perception.

mmWave Image Simulators. Given the growth in millimeter wave devices for networking and sensing, the vast majority of existing millimeter wave simulations have also focused on understanding channel characteristics (e.g., for 5G networks) [8, 33, 41] or for imaging humans for action recognition and HCI applications [47, 50, 52]. In principle, these simulators could be used also for generating mmWave images of everyday objects; however, existing simulators are extremely expensive, costing tens of thousands of dollars [8] and/or are limited to simulating metallic items and cannot simulate everyday objects with different properties [38]. In contrast, we developed an open-source simulator and demonstrated that it generates synthetic data that matches real-world collected data. We believe that this tool combined with advances in vision algorithms can lead to very high accuracy in non-line-of-sight scenarios.

mmWave Perception. Prior work has demonstrated the use of millimeter waves for various perception tasks, including detection and classification. However, these approaches are limited to specific domains, such as vehicles [22, 29, 42], pedestrians [24], weapons [39, 40], or entirely metallic objects [30]. Through a new dataset and simulator, our work aims to expand the application of mmWave perception to a more open domain consisting of diverse categories.

3. Background

In this section, we provide a high-level overview on mmWave imaging and its properties.

3.1. mmWave Imaging

A mmWave radar transmits wireless signals with millimeter-wave wavelengths, captures their reflections, and uses them to generate 3D images, as shown in Fig. 2a. It uses two core signal processing techniques. First, it estimates the distance of each reflection by comparing the frequency between the transmitted and received signals. Second, it measures the angle of reflection (in both azimuth and elevation) by comparing the received signals between

different antennas. 3D images can then be performed by calculating the reflection power emanating from each voxel in 3D space.

The captured image can be represented as a heatmap as shown in Fig. 2b, where red represents high intensity reflection and blue represents low intensity. It is important to note that this visualization is a 2D projection of the 3D image. Mathematically, since every sample from the radar is a complex number with a phase and an amplitude, we can combine them with the following equation:

$$I(x, y, z) = \sum_{k=1}^K \sum_{j=1}^N S_{j,k} e^{\frac{j2\pi d(x,y,z,k)}{\lambda_j}} \quad (1)$$

where $I(x, y, z)$ is the complex mmWave image at location (x, y, z) , K is the number of antennas, N is the number of samples in each signal, $S_{j,k}$ is the j^{th} sample of the received signal from the k^{th} antenna, and λ_j is the wavelength of the signal at sample j , which is proportional to the speed of light c and the frequency f as $\lambda = \frac{c}{f}$. $d(x, y, z, k) = 2\|(x, y, z) - p_k\|$ is the round-trip distance from the k^{th} antenna (at location p_k) to the point (x, y, z) .

3.1.1. Resolution

One important characteristic of a mmWave image is its resolution. The resolution in range (depth) is determined by the *bandwidth*, or the range of frequencies that the signal covers. We compute the depth resolution δ_z as:

$$\delta_z = \frac{c}{2B} \quad (2)$$

where c is the speed of light, and B is the bandwidth of the signal. The resolution in the horizontal and vertical dimensions is dependent on the *aperture*, or the distance between the first and last antenna in that dimension.

$$\delta_x = \frac{\lambda z_0}{2D_x} \quad \delta_y = \frac{\lambda z_0}{2D_y} \quad (3)$$

where δ_x and δ_y are the resolution in the x and y dimensions, respectively. z_0 is the range to the target, and D_x and D_y are the apertures in x and y dimensions, respectively.

3.1.2. Synthetic Aperture Radar (SAR) Imaging

As described above, it is desirable to increase the aperture to increase the image resolution (Eq. 3). Instead of creating a large aperture through a large number of physical antennas on the radar, it is possible to perform SAR imaging. In this method, one set of transmitters/receivers are moved through the environment, taking measurements from different locations, and constructing a “synthetic aperture”. These measurements can be combined through Eq. 1 to provide the same resolution as a physical aperture.

3.2. Impact of Frequency

One important question is what frequency to use for imaging. The frequency introduces an important tradeoff. First, higher frequencies result in higher resolution (as seen in

Eq. 3). On the other hand, higher frequency signals experience more attenuation, or power loss, as they travel through materials [5]. This means that high frequency signals may have higher noise through thick occlusions than lower frequencies. This is why our dataset and simulator include multi-spectral (multi-frequency) mmWave images.

When selecting frequencies, we chose mmWave signals because lower frequencies (e.g., WiFi) have poor resolution [9], while higher ones (e.g., Terahertz) struggle with occlusions [17]. In mmWave spectrum, we selected 24 GHz and 77 GHz since these are the bands approved by the FCC for industrial and commercial use [20] and most commercial mmWave radars operate within them.

3.3. Types of Reflections

mmWave signals primarily exhibit specular (mirror-like) reflections [32], as illustrated in Fig. 3. Due to the significantly longer wavelengths of mmWave signals compared to visible light (millimeters vs nanometers), surfaces that appear diffuse (i.e., omnidirectional) for visible light (blue) often appear specular for mmWave signals (red).

In addition to specular reflections, mmWaves also exhibit strong reflections when a wave strikes a sharp edge, scattering it in multiple directions. These reflections, known as edge diffraction, can impact signal propagation and perception differently from diffuse or specular reflections.

These reflection properties are one fundamental difference between mmWave signals and visible light that necessitates algorithms and models specifically designed for mmWave images.

4. MITO Dataset

In this section, we describe the design choices and process of creating MITO. The dataset consists of over 24 million mmWave frames (where each frame is a complex-valued time series). We used these frames to generate 550 unique, high-resolution 3D mmWave SAR images of 76 diverse objects.

4.1. Object Selection

MITO builds on the YCB dataset [14], a standard dataset of everyday objects used for robotic manipulation. We select 76 out of 80 objects from the YCB dataset (the remaining 4 were discarded due to not being able to obtain the exact object). Unlike previous mmWave datasets, these objects cover a diverse range of shapes, sizes, materials, and categories.³ The YCB dataset also provides 2D images and 3D object meshes, which we use to simulate mmWave images.

4.2. Data Collection Protocol

4.2.1. Real-World mmWave Images

Fig. 1 visualizes our data collection setup. We connect a 77 GHz radar (TI IWR1443Boost [6] and

³Additional details on object diversity are provided in supplementary.

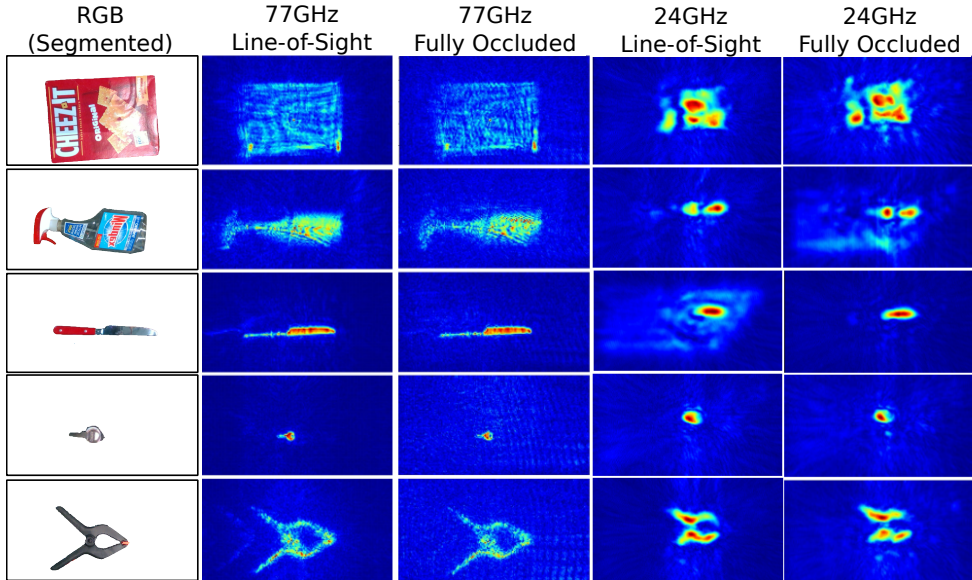


Figure 4. **Sample Images.** A number of example mmWave images within MITO.

DCA1000EVM [1]), 24 GHz radar (Infineon Position2Go [4]), and Intel Realsense D415 [25] to an end-effector of a UR5e robotic arm [44] using custom-designed 3D-printed parts. Since the robot and radars are controlled from different computers, we synchronize them by setting both computers to the same NTP time server.

We place the objects in two setups that minimize background reflections in different ways. In the first, we fix each object onto a tripod by hot-gluing a 3D-printed nut to each object and screwing it onto a threaded tripod. Because there is no surface directly below the object, any strong reflections from the background are avoided. In the second, we place the object directly on a styrofoam block, since styrofoam is largely transparent to mmWave signals [7]. We also include experiments where the tripod/styrofoam is placed in the scene without any objects so that the impact of the tripod/styrofoam can be removed by subtracting the empty image from the main image [10].

At the start of an experiment, the robot moves the camera to the middle of the workspace to take an RGB-D image prior to any potential occlusion (i.e., in the NLOS scenario). Then, it moves the radars throughout the workspace, covering a rectangular space. The aperture of our experiments range from 55cm by 22cm to 60cm by 45cm, ensuring that each experiment uses an aperture which covers the full object. The radars continuously measure mmWave signals while the robot is moving, and the robot records its trajectory over time. After we complete an experiment in LOS, we run an experiment in NLOS without moving the object. We place a layer of cardboard over the object to simulate the case where the object was placed inside a box. We also collect experiments with four layers of fabric over the cardboard to simulate more dense occlusions.

4.2.2. Synthetic mmWave Images

In addition to the real-world data, we also provide a simulation tool to generate synthetic mmWave images, which can be used to increase the volume of data to aid in model training. We include at least 2 different simulation images for each object, along with the simulator itself for producing additional images (see Sec. 5 for more details).

4.3. Data Processing

To process a real-world mmWave image, we need to know the location where each measurement was taken. To do this, we interpolate the timestamped robot locations to match the timestamp of the radar measurements. The interpolated locations, in addition to the raw radar measurements, are then processed into a 3D mmWave image by applying Eq. 1. Example images can be seen in Fig. 4, which shows the segmented RGB images (1st column), 77 GHz LOS (2nd column), 77 GHz NLOS (3rd column), 24 GHz LOS (4th column), and 24 GHz NLOS (5th column) mmWave images. Additional images are provided in the supplementary.

We produce 550 3D, complex-valued mmWave images at two different frequencies (24 GHz & 77 GHz) in both LOS and NLOS settings using 24 million raw measurements and locations. We include the raw data in MITO to enable flexibility in leveraging and/or postprocessing the data using a custom pipeline. We also include images of objects at different angles and images with multiple objects.

For each mmWave image, we use its corresponding RGB-D image (in LOS) to provide a ground truth object segmentation mask. The segmentation masks are produced by using an interactive interface for the segment-anything model (SAM) [27] to select the points on the RGB picture as a prompt for the model. The human annotator continues selecting points until the mask covers the full object. We

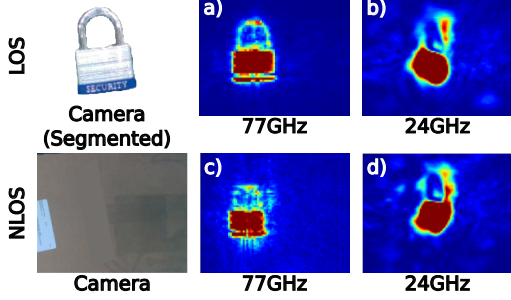


Figure 5. **Multi-Spectral Imaging.** a-b) show 77 GHz & 24 GHz images for a padlock in LOS. c-d) show the images in NLOS.

then use the camera’s location to transform and align the RGB-D ground-truth mask with the mmWave image. More details on the alignment process are in the supplementary.

4.4. Analysis of Different Frequencies

Recall from Sec. 3.2 that the frequency of the mmWave signal impacts both the resolution of the resulting image and the ability for the signal to traverse through occlusions. We analyze this phenomenon in real-world images in MITO in Fig. 5. Fig.5a-b show a 77 GHz and 24 GHz image of a padlock in LOS, respectively. The 77 GHz image is higher resolution, as expected. On the other hand, Fig. 5c-d show 77 GHz and 24 GHz images of the same object in NLOS (placed underneath cardboard). In this case, the 24 GHz image is very similar to the LOS case, while the 77 GHz shows some artifacts that were not present in LOS. This is because the 24 GHz signal travels through the cardboard relatively unaffected, while the 77 GHz is partially reflected and absorbed. We hope that by including two different frequencies, future algorithms can leverage both images to benefit from high-resolution and robustness to occlusions.

5. MITO Simulator

In this section, we describe our open-source mmWave image simulator, and evaluate the simulator’s accuracy.

5.1. mmWave Simulation

Our simulator takes as input a 3D triangle mesh and radar locations to simulate mmWave signals from. The mesh files can be sourced from object datasets (e.g., YCB [14]), online repositories (e.g., 3D Warehouse, Turbo Squid), or custom-generated on smartphones (e.g., PolyCam iPhone app).

At a high level, our simulator works by estimating the raw signals expected at each of these locations, given reflections off the target object. Then, synthetic images are produced by feeding these simulated signals into the same image processing pipeline used for real world data (Eq. 1).

Estimating raw signals at a given location is as follows:

1. First, we find which mesh vertices in the mesh are visible from that location [3].
2. Next, for a given visible vertex, we measure the distance

to the measurement location. Given the distance, we simulate the reflection from this vertex:

$$s_j(l, v) = e^{-j \frac{4\pi|l-v|}{\lambda_j}} \quad (4)$$

where $s_j(l, v)$ is the j^{th} sample of the reflection from location l to vertex v and back.

3. Finally, we sum the simulated reflections from all visible vertices to produce the raw signal for this measurement location. Formally:

$$S_j = \sum_{v \in V} s_j(l, v) \quad (5)$$

where S_j is the j^{th} sample of the simulated signal from measurement location l , V is the set of visible vertices.

After repeating this for each measurement location, we feed the raw signals through our imaging processing pipeline to produce the final synthetic image. Note that we can rotate the mesh files to produce synthetic images at various angles.

Recall from Sec. 3.3 that the object’s material and texture may result in different types of reflections. To accurately model different objects, we introduce 2 variations of the simulation to account for different types of reflections.

5.1.1. Specular Reflections

When an object exhibits purely specular reflections, the signal will reflect off each vertex in only one direction. In some cases, the signal is reflected away from the radar’s receivers, and therefore should not be added to S_j . Specifically, the signal will only be reflected back towards the radar if the surface normal is pointing towards the radar’s location. Otherwise, the signal will be reflected away from the receiver.

We update our above simulation to account for this by removing reflections where the angle between the normal (\mathbf{n}) and the vector from the radar to the vertex ($l - v$) is less than a threshold τ . Formally, we can update Eq. 4 to:

$$s_j(l, v) = \begin{cases} 0 & \cos^{-1}\left(\frac{\mathbf{n} \cdot (l-v)}{\|\mathbf{n}\| \|l-v\|}\right) \geq \tau \\ e^{-j \frac{4\pi|l-v|}{\lambda_j}} & \cos^{-1}\left(\frac{\mathbf{n} \cdot (l-v)}{\|\mathbf{n}\| \|l-v\|}\right) < \tau \end{cases} \quad (6)$$

Fig. 6b shows an example when simulating entirely based on specular reflections.

5.1.2. Edge Reflections

In other cases, the signal experiences scattering effects from the edges of objects. First, we define a vertex as being on an edge of an object when the angle between two of its faces is greater than an angle τ_e , and we find the set of all vertices that lie on an edge, V_e .

Then, we replace Eq. 4 such that it only allows reflections from edge vertices.

$$s_j(l, v) = \begin{cases} 0 & v \notin V_e \\ e^{-j \frac{4\pi|l-v|}{\lambda_j}} & v \in V_e \end{cases} \quad (7)$$

Fig. 6c shows an example when simulating edge reflections.

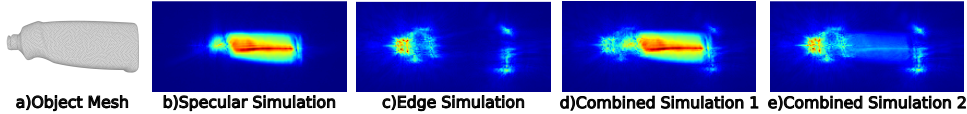


Figure 6. **Simulation Output.** Our simulation uses a) a 3D mesh to produce images assuming different reflection types: b) specular & c) edge. d/e) We combine these with different weights to simulate different materials.

Simulation	25 th	50 th	75 th
Combined	85%	94%	98%
Specular	68%	90%	97%
Edge	49%	71%	88%

Table 1. **Simulation 3D F-Score** for combined, specular, & edge simulations

5.1.3. Combing Reflections

In practice, materials rarely exhibit only one type of reflection, but instead some combination of the two. To account for this, our synthetic images can be added together with different weights to simulate different materials:

$$I_{syn}(\alpha_1, \alpha_2) = \frac{\alpha_1}{\alpha_1 + \alpha_2} I_s + \frac{\alpha_2}{\alpha_1 + \alpha_2} I_e \quad (8)$$

where $I_{syn}(\alpha_1, \alpha_2)$ is the combined synthetic image for weights α_1, α_2 , and I_s and I_e are the images from the specular and edge simulations, respectively. Fig. 6d-e shows two examples of combining simulations with different weights representing two different materials.

5.2. Simulation Accuracy

To evaluate the accuracy of our simulator, we use the standard 3D F-score metric [43] to compare the mmWave outputs from real-world and simulation.

5.2.1. Aligning the Point Clouds

Before we compute the 3D F-score, we first need to convert both the real-world and simulation images to a point cloud. To do so, we apply a standard mmWave point cloud generation procedure[18] by creating one point in the center of each mmWave voxel that has a power above a threshold τ_P :

$$P_R = \{p \mid |I(p)| > \tau_P\} \quad P_S = \{p \mid |I_{syn}(p)| > \tau_P\}$$

where P_R and P_S are the set of points created for the real and synthetic mmWave images, respectively.

Next, we align the real-world and simulation point clouds using a standard iterative closest point implementation [2]. This is necessary because our mmWave simulation places the object in the center of the image, while our real world experiments may have objects offset from the center.

5.2.2. 3D F-Score

We evaluate the point cloud similarity using a standard metric, 3D F-score [43], defined as:

$$PR = \frac{1}{N_R} \sum_{i=1}^{N_R} \mathbb{1}_{d(P_R(i), P_S) < \tau_F} \quad (9)$$

$$RE = \frac{1}{N_S} \sum_{j=1}^{N_S} \mathbb{1}_{d(P_S(j), P_R) < \tau_F}, \quad F = \frac{2 PR RE}{PR + RE} \quad (10)$$

where PR , RE , and F are the precision, recall, and F-score. $\mathbb{1}$ is an indicator variable. N_R (N_S) is the number of points in the real (synthetic) point cloud. τ_F is the F-score distance threshold. $d(x, P)$ is the distance from point x to its nearest neighbor in cloud P : $d(x, P) = \min_{x' \in P} \|x - x'\|$.

Since our goal is not to select a single set of weights for each object, but to allow the simulation to represent many different objects, we compute this metric across a range of weights $\{\alpha_1, \alpha_2\}$ and choose the combined simulation which produces the best F-score (e.g., the simulation which best matches the properties of this real-world object).

$$F = \max_{(\alpha_1, \alpha_2) \in W} F(I_{syn}(\alpha_1, \alpha_2), I) \quad (11)$$

where $F(I_{syn}, I)$ is the F-score for a synthetic image I_{syn} and real-world image I , and W is the set of all weights.

5.2.3. Results

We use the above process to compute the 3D F-score for all objects in the dataset. We also compare to the accuracy when using only specular simulation images (i.e., $\alpha_1 = 1, \alpha_2 = 0$), and when using only edge simulation images (i.e., $\alpha_1 = 0, \alpha_2 = 1$).

Table 1 reports the 25th, 50th, and 75th percentile F-scores for MITO (1st row), specular only (2nd row) and edge only (3rd row). MITO’s simulator achieves a median F-score of 94%, while the specular-only or edge-only simulators achieve median F-scores of 90% and 71%, respectively. An even larger improvement can be seen in the 25th percentile (85% vs 68% and 49%). This shows the value of MITO’s techniques for combining multiple simulation types.

6. Non-Line-of-Sight Applications

In this section, we evaluate the ability of our dataset and simulator to enable and establish baselines for NLOS perception for diverse, everyday objects. We describe our experimental setup and analyze the evaluation metrics for NLOS segmentation and classification.

Such applications would be useful in a variety of areas, such as confirming customer orders are properly packaged in e-commerce warehouses, detecting broken objects during shipping, and efficiently finding objects for robotic search.

6.1. Object Segmentation

We show how MITO can be used to build a mmWave object segmentation tool that works in LOS and NLOS.

6.1.1. Setup

We build on the state-of-the-art segment-anything model (SAM) [27], which takes as input an image to segment and a prompt, either in the form of points in the image or a bounding box. The model returns one or multiple masks, and a score associated with the predicted mask quality.

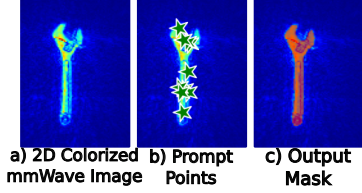


Figure 7. **Segmentation** a)Colorize 2D image b)Select prompt points c)Segment with SAM

Input	LOS					NLOS				
	Pre.	Recall	F1	IoU	Acc.	Pre.	Recall	F1	IoU	Acc.
Camera	99.7%	99.5%	99.4%	98.9%	99.9%	3.6%	100%*	7.0%	3.6%	14.0%
24 GHz	57.9%	50.1%	37.3%	22.9%	93.7%	53.0%	38.7%	29.1%	17.0%	92.1%
77 GHz	98.2%	56.4%	71.4%	55.5%	97.9%	95.4%	57.7%	70.2%	54.1%	97.7%
Multi Spectral	97.1%	62.6%	74.4%	59.3%	98.0%	95.1%	63.1%	70.8%	54.9%	97.6%

Table 2. **Segmentation Accuracy.** Precision (Pre), Recall, F1 Score, IoU, and Accuracy (Acc) when segmenting camera, 24 GHz, 77 GHz, and multi-spectral images, in both LOS and NLOS scenarios.

Directly using an off-the-shelf object segmentation network for mmWave images faces two challenges. First, SAM is trained on 2D RGB images, but mmWave images are single-channel, complex-valued, and 3D. Second, the SAM model requires a prompt before returning segmentation masks. We note that while there are fully automatic methods using SAM (e.g., iterating through a grid of points as a prompt)[27], they aim to provide all masks within an image, and would not be applicable in our case since they do not identify which mask contains the object of interest.

To convert our mmWave images to 2D RGB images, we start by averaging the magnitudes along the depth of the 3D image, and use a rainbow colormap for colorization, as shown in Fig. 7a. Second, we randomly select a subset of the highest power reflection points as prompts, as shown in Fig. 7b. By feeding the resulting RGB image and prompts to the SAM network, we can obtain mmWave segmentation masks as shown in Fig. 7c. We apply the same approach for segmenting both 24 GHz and 77 GHz images. Additional details can be found in the supplementary.

Multi-Spectral Images. Beyond segmenting 77 GHz and 24 GHz images separately, we also propose a method for fusing the two images to improve overall segmentation accuracy. To do so, we combine the images during prompt point selection: instead of using a power threshold based only on a single image, the points must exceed thresholds in both 24 GHz and 77 GHz images. Then, we use these points and the 77 GHz colorized image as input to the SAM network. This allows the 24 GHz image to act as a filter, removing the impact of noise (e.g., from cardboard occluders) on the point selection and improving segmentation quality.

6.1.2. Experiments

Baseline. We compare our segmentation performance to an RGB-D camera baseline. We use the camera image from the experiment directly as input to the SAM model. To select prompt points, we use the depth image to automatically filter out pixels greater than a certain depth (i.e., the background), and randomly select prompt points from the remaining pixels. In the LOS scenarios, this corresponds to points on the object. In NLOS scenarios, this corresponds to points on the occluding object (i.e., the cardboard).

Quantitative Results. Tab. 2 shows the median Precision, Recall, F-score, Intersection-over-Union (IoU), and Accuracy when using the camera, 24 GHz, 77 GHz, and

multi-spectral (24 GHz & 77 GHz) images for both LOS and NLOS scenarios. In LOS, segmenting camera images achieves a median precision, recall and F-score of 99.7%, 99.5%, and 99.4%, respectively. However, in NLOS, the camera only achieves 3.6% precision and 7.0% F-score, which is expected since cameras (and other visible-light-based sensors) are unable to operate through occlusions. We note that the camera still achieves 100% recall since SAM segments the cardboard occluder, covering the full object.

In contrast, the various mmWave image inputs achieve better performance in NLOS scenarios, demonstrating how MITO enables NLOS object segmentation. In particular, the F-score of NLOS for 24 GHz, 77 GHz, and multi-spectral exceeds that of the camera. Notably, multi-spectral images achieve the highest performance. When comparing LOS and NLOS, multi-spectral images only experience a 2.0%, 0.5%, and 3.6% change in precision, recall, and F-score, respectively. This demonstrates that MITO is able to accurately image and perceive fully occluded objects with a similar performance as in LOS.

Interestingly, the recall when segmenting mmWave images is lower (63.1%) than the precision (95.1%). This is primarily because mmWaves are specular, as described earlier, preventing certain portions of the object from appearing in the image. We provide a more detailed discussion on this phenomenon in the supplementary and Sec. 6.3 highlight how future work can improve recall via shape completion.

The IoU and accuracy reported in Table 2 show similar trends. Notably, 24 GHz, 77 GHz, and multi-spectral all outperform the camera in NLOS. We also note that the accuracy is high because it is dominated by the background.

Qualitative Results. In some cases, the depth camera is unable to measure the depth to every point on the object. This is typically the case for very reflective objects (e.g., mirror-like metallic objects) or clear objects (e.g., glass or plastic). In these cases, MITO is able to reconstruct more of the object than the depth camera, as shown in Fig. 8. In Fig. 8b, the image from the depth camera has holes due to the object’s material reflectivity, whereas in Fig. 8c, MITO’s mmWave image captures the whole object. Fig. 8d shows our 77 GHz mmWave segmentation masks the entire object.

6.2. Sim2Real Shape Classification

Next, we demonstrate how MITO can be used to classify objects in NLOS based on their geometry.

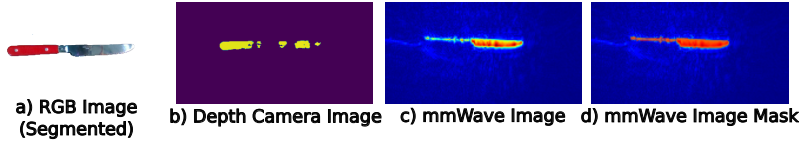


Figure 8. **Qualitative Segmentation Result.** An example where the depth image is unable to capture the entire object, but the mmWave image does.

6.2.1. Setup

We design a classifier which takes 77 GHz mmWave images (after applying the segmentation mask from Sec. 6.1) as input, and outputs the estimated class label. The classifier is a neural network consisting of 5 convolutional layers, followed by 3 fully connected layers, and a softmax activation. We *train the classifier entirely on synthetic data*, and *evaluate on real-world images* in both LOS and NLOS. To generate synthetic images for training, we leverage object meshes provided by YCB dataset.

One challenge in training from synthetic images is to determine which types of reflections dominate for a given object. Recall from Sec. 5 that our simulator models two different reflection types. However, it is difficult to accurately measure the material/texture properties of all objects to identify how to correctly combine these simulation images. Instead, we introduce a new data augmentation, where we choose random weights for each simulation type and sum the weighted images. This allows the network to train on different material properties for each object. We also apply standard image augmentations (rotation, translation, masking, blur). More training details are in supplementary.

6.2.2. Experiments

We report the shape classification results on real-world data in LOS and NLOS in Tab. 3. Our classifier performs with an overall accuracy of 85.2%. Specifically, it achieves an accuracy of 88.8% and 81.2% for LOS and NLOS scenarios, respectively, showing that MITO can be used to enable novel capabilities such as NLOS shape classification.

In Tab. 3, we also include results using a classifier trained on either only edge images (i.e., without combining them with the specular images) or only specular images in order to evaluate the impact of our different simulation types on the classifier accuracy. We observe that these models are only able to achieve 67.6% and 76.4%, whereas using both simulation types together achieves 85.2% accuracy. This shows the benefit of our simulator’s different outputs, and our data augmentation technique to combine them.

These results shows that MITO has the potential to be used for novel NLOS applications, such as confirming packaged orders in closed boxes. Furthermore, by training on synthetic images and evaluating on real-world data, we show that our simulator is representative of the real-world.

Training Data		Accuracy		
Edge	Specular	LOS	NLOS	Overall
X		61.1%	75.0%	67.6%
	X	77.7%	75.0%	76.4%
X	X	88.8%	81.2%	85.2%

Table 3. **Classifier Accuracy** for LOS, NLOS, & overall using specular, edge, & combined simulations for training.

6.3. Additional NLOS Applications & Extensions

In addition to the applications described above, MITO also paves the way for future work in multiple directions:

- *NLOS Object Completion:* In some cases, the mmWave images do not capture the entire object due to specularity (See supplementary for more details). It would be interesting future work to create an object completion network that learns the missing parts of an object & creates more photo-realistic NLOS images.
- *NLOS 6DoF Estimation:* Another interesting problem is 6DoF estimation from mmWave images. This could be used to ensure proper liquid packaging to avoid spills, or enable efficient grasp planning in NLOS (e.g., grasping an item under cloth or within a box with packing peanuts).
- *NLOS Robotic Manipulation:* Future work can leverage many of the above NLOS perception tasks to enable new tasks in robotic manipulation. For example, accurate mmWave object segmentation and classification can significantly increase the efficiency of mechanical search and retrieval (i.e., the problem of searching for a specific item in clutter). Further, mmWave images can be used to analyze pile stability to improve push and grasp planners. NLOS perception can also help autonomous robots determine which packages contain fragile materials to be handled with special care. More generally, NLOS perception can help autonomous robots to operate in more realistic, cluttered environments.

7. Conclusion

We present MITO, the first millimeter-wave (mmWave) dataset of diverse, everyday objects in both line-of-sight and fully-occluded settings. We collect over 24 million frames of mmWave images, and used them to synthesize 550 high-resolution real world 3D (SAR) mmWave images for 76 objects. We also develop an open-source simulator that can be used to generate synthetic images for any 3D mesh. We demonstrate the utility of our contributions in two applications – NLOS object segmentation and NLOS shape classification – establishing baselines for future research and paving the way for important applications in robotic perception, logistics, scene understanding.

As the research evolves, it would be interesting to expand the dataset – incorporating additional items, surfaces, occlusion types, etc. – which would continue improving the accuracy of the demonstrated NLOS tasks and unlock additional ones. More generally, we hope this work serves as a

foundation and motivation for future research in mmWave-based NLOS perception, similar to how early RGB datasets accelerated the research in optical-based Computer Vision, and continued driving the field forward as they expanded.

References

- [1] Ti dca1000evm. <https://www.ti.com/tool/DCA1000EVM>. 4
- [2] Icp registration. https://www.open3d.org/docs/release/tutorial/pipelines/icp_registration.html. 6
- [3] Perceiving systems mesh package. <https://ps.is.mpg.de/code/mesh-library>. 5
- [4] Infineon position2go. <https://www.infineon.com/cms/en/product/evaluation-boards/demo-position2go/>. 4
- [5] Understanding mmwave for 5g networks. <https://www.5gamericas.org/wp-content/uploads/2020/12/InDesign-Understanding-mmWave-for-5G-Networks.pdf>. 3
- [6] Ti iwr1443boost. <https://www.ti.com/product/IWR1443#tech-docs>. 1, 3
- [7] mmWave Radar Radome Design Guide. <https://www.ti.com/lit/an/swra705/swra705.pdf>, 2021. Texas Instruments. 4
- [8] Ansys high frequency structure simulator (hfss), 2022. Ansys HFSS. 2
- [9] Fadel Adib, Zach Kabelac, Dina Katabi, and Robert C Miller. 3d tracking via body radio reflections. In *11th USENIX Symposium on Networked Systems Design and Implementation (NSDI 14)*, pages 317–329, 2014. 3
- [10] Fadel Adib, Chen-Yu Hsu, Hongzi Mao, Dina Katabi, and Frédo Durand. Capturing the human figure through a wall. *ACM Transactions on Graphics (TOG)*, 34(6):219, 2015. 4
- [11] Mario Bijelic, Tobias Gruber, Fahim Mannan, Florian Kraus, Werner Ritter, Klaus Dietmayer, and Felix Heide. Seeing through fog without seeing fog: Deep multimodal sensor fusion in unseen adverse weather. In *The IEEE Conference on Computer Vision and Pattern Recognition (CVPR)*, 2020. 2
- [12] Walter Brescia, Pedro Gomes, Laura Toni, Saverio Mascolo, and Luca De Cicco. Millinoise: a millimeter-wave radar sparse point cloud dataset in indoor scenarios. In *Proceedings of the 15th ACM Multimedia Systems Conference*, pages 422–428, 2024. 2
- [13] H. Caesar, V. Bankiti, A. H. Lang, S. Vora, V. Liong, Q. Xu, A. Krishnan, Y. Pan, G. Baldan, and O. Beijbom. nusenes: A multimodal dataset for autonomous driving. In *2020 IEEE/CVF Conference on Computer Vision and Pattern Recognition (CVPR)*, pages 11618–11628, Los Alamitos, CA, USA, 2020. IEEE Computer Society. 2
- [14] Berk Calli, Arjun Singh, James Bruce, Aaron Walsman, Kurt Konolige, Siddhartha Srinivasa, Pieter Abbeel, and Aaron M Dollar. Yale-cmu-berkeley dataset for robotic manipulation research. *The International Journal of Robotics Research*, 36(3):261–268, 2017. 2, 3, 5
- [15] Anjun Chen, Xiangyu Wang, Shaohao Zhu, Yanxu Li, Jiming Chen, and Qi Ye. mmbody benchmark: 3d body reconstruction dataset and analysis for millimeter wave radar, 2022. 2
- [16] Han Cui, Shu Zhong, Jiacheng Wu, Zichao Shen, Naim Dahoun, and Yiren Zhao. Milipoint: A point cloud dataset for mmwave radar, 2023. 2
- [17] Pham Tien Dat, Yuya Yamaguchi, Shingo Takano, Shotaro Hirata, Junichiro Ichikawa, Ryo Shimizu, Keizo Inagaki, Isao Morohashi, Yuki Yoshida, Atsushi Kanno, Naokatsu Yamamoto, Tetsuya Kawanishi, and Kouichi Akahane. Terahertz signal transparent relay and switching using photonic technology. *Journal of Lightwave Technology*, 42(3):1173–1182, 2024. 3
- [18] Laura Dodds, Hailan Shanbhag, Junfeng Guan, Saurabh Gupta, and Haitham Hassanieh. Around the corner mmwave imaging in practical environments. In *Proceedings of the 30th Annual International Conference on Mobile Computing and Networking*, pages 1–15, 2024. 6
- [19] M. Everingham, L. Van Gool, C. K. I. Williams, J. Winn, and A. Zisserman. The pascal visual object classes (voc) challenge. *International Journal of Computer Vision*, 88(2): 303–338, 2010. 2
- [20] Federal Communications Commission. Frequency Allocation: transition.fcc.gov/oet/spectrum/table/fcctable.pdf. 3
- [21] Simon Fothergill, Helena Mentis, Pushmeet Kohli, and Sebastian Nowozin. Instructing people for training gestural interactive systems. In *Proceedings of the SIGCHI Conference on Human Factors in Computing Systems*, page 1737–1746, New York, NY, USA, 2012. Association for Computing Machinery. 2
- [22] Junfeng Guan, Sohrab Madani, Suraj Jog, Saurabh Gupta, and Haitham Hassanieh. Through fog high-resolution imaging using millimeter wave radar. In *IEEE/CVF Conference on Computer Vision and Pattern Recognition (CVPR)*, 2020. 2
- [23] Runwei Guan, Ruixiao Zhang, Ningwei Ouyang, Jianan Liu, Ka Lok Man, Xiaohao Cai, Ming Xu, Jeremy Smith, Eng Gee Lim, Yutao Yue, et al. Talk2radar: Bridging natural language with 4d mmwave radar for 3d referring expression comprehension. *arXiv preprint arXiv:2405.12821*, 2024. 2
- [24] Siddharth Gupta, Prabhat Kumar Rai, Abhinav Kumar, Phaneendra K. Yalavarthy, and Linga Reddy Cenkeramaddi. Target classification by mmwave fmcw radars using machine learning on range-angle images. *IEEE Sensors Journal*, 21(18):19993–20001, 2021. 2
- [25] Intel RealSense. <https://www.intelrealsense.com>, 2019. 4
- [26] Allison Janoch, Sergey Karayev, Yangqing Jia, Jonathan T. Barron, Mario Fritz, Kate Saenko, and Trevor Darrell. A category-level 3-d object dataset: Putting the kinect to work. In *2011 IEEE International Conference on Computer Vision Workshops (ICCV Workshops)*, pages 1168–1174, 2011. 2
- [27] Alexander Kirillov, Eric Mintun, Nikhila Ravi, Hanzi Mao, Chloe Rolland, Laura Gustafson, Tete Xiao, Spencer Whitehead, Alexander C. Berg, Wan-Yen Lo, Piotr Dollár, and

- Ross Girshick. Segment anything. *arXiv:2304.02643*, 2023. 2, 4, 6, 7
- [28] Andrew Kramer, Kyle Harlow, Christopher Williams, and Christoffer Heckman. Coloradar: The direct 3d millimeter wave radar dataset. *The International Journal of Robotics Research*, 41(4):351–360, 2022. 2
- [29] Mohamed Lamane, Mohamed Tabaa, and Abdessamad Klilou. Classification of targets detected by mmwave radar using yolov5. *Procedia Computer Science*, 203:426–431, 2022. 17th International Conference on Future Networks and Communications / 19th International Conference on Mobile Systems and Pervasive Computing / 12th International Conference on Sustainable Energy Information Technology (FNC/MobiSPC/SEIT 2022), August 9-11, 2022, Niagara Falls, Ontario, Canada. 2
- [30] Jie Liu, Kai Zhang, Zhenlin Sun, Qiang Wu, Wei He, and Hao Wang. Concealed object detection and recognition system based on millimeter wave fmcw radar. *Applied Sciences*, 11(19), 2021. 2
- [31] Ting Liu, Yao Zhao, Yunchao Wei, Yufeng Zhao, and Shikui Wei. Concealed object detection for activate millimeter wave image. *IEEE Transactions on Industrial Electronics*, 66(12):9909–9917, 2019. 2
- [32] Jonathan S. Lu, Patrick Cabrol, Daniel Steinbach, and Ravikumar V. Pragada. Measurement and characterization of various outdoor 60 ghz diffracted and scattered paths. In *MILCOM 2013 - 2013 IEEE Military Communications Conference*, pages 1238–1243, 2013. 3
- [33] Marco Mezzavilla, Menglei Zhang, Michele Polese, Russell Ford, Sourjya Dutta, Sundeep Rangan, and Michele Zorzi. End-to-end simulation of 5g mmwave networks. *IEEE Communications Surveys & Tutorials*, 20(3):2237–2263, 2018. 2
- [34] Dong-Hee Paek, Seung-Hyun Kong, and Kevin Tirta Wijaya. K-radar: 4d radar object detection for autonomous driving in various weather conditions. In *Thirty-sixth Conference on Neural Information Processing Systems Datasets and Benchmarks Track*, 2022. 2
- [35] Andras Palfy, Ewoud Pool, Srimannarayana Baratam, Julian F. P. Kooij, and Dariu M. Gavrila. Multi-class road user detection with 3+1d radar in the view-of-delft dataset. *IEEE Robotics and Automation Letters*, 7(2):4961–4968, 2022. 2
- [36] Akarsh Prabhakara, Tao Jin, Arnav Das, Gantavya Bhatt, Lilly Kumari, Elahe Soltanaghahi, Jeff Bilmes, Swarun Kumar, and Anthony Rowe. Radarhd: Demonstrating lidar-like point clouds from mmwave radar. In *Proceedings of the 29th Annual International Conference on Mobile Computing and Networking*, pages 1–3, 2023. 2
- [37] M Mahbubur Rahman, Ryoma Yataka, Sorachi Kato, Pu Perry Wang, Peizhao Li, Adriano Cardace, and Petros Boufounos. Mmvr: Millimeter-wave multi-view radar dataset and benchmark for indoor perception. *arXiv preprint arXiv:2406.10708*, 2024. 2
- [38] Hem Regmi, Moh Sabbir Saadat, Sanjib Sur, and Srihari Nelakuditi. Squigglemilli: Approximating sar imaging on mobile millimeter-wave devices. *Proc. ACM Interact. Mob. Wearable Ubiquitous Technol.*, 5(3), 2021. 2
- [39] Bofeng Su and Minghui Yuan. Object recognition for millimeter wave mimo-sar images based on high-resolution feature recursive alignment fusion network. *IEEE Sensors Journal*, 23(14):16413–16427, 2023. 2
- [40] Peng Sun, Ting Liu, Xiaotong Chen, Shiyin Zhang, Yao Zhao, and Shikui Wei. Multi-source aggregation transformer for concealed object detection in millimeter-wave images. *IEEE Transactions on Circuits and Systems for Video Technology*, 32(9):6148–6159, 2022. 2
- [41] Shu Sun, George R MacCartney, and Theodore S Rappaport. A novel millimeter-wave channel simulator and applications for 5g wireless communications. In *2017 IEEE international conference on communications (ICC)*, pages 1–7. IEEE, 2017. 2
- [42] Y. Sun, Z. Huang, H. Zhang, Z. Cao, and D. Xu. 3drimr: 3d reconstruction and imaging via mmwave radar based on deep learning. In *2021 IEEE International Performance, Computing, and Communications Conference (IPCCC)*, pages 1–8, Los Alamitos, CA, USA, 2021. IEEE Computer Society. 2
- [43] Maxim Tatarchenko*, Stephan R. Richter*, René Ranftl, Zhuwen Li, Vladlen Koltun, and Thomas Brox. What do single-view 3d reconstruction networks learn? 2019. 6
- [44] Universal Robots, UR5e. <https://www.universal-robots.com/products/ur5-robot/>, 2021. 4
- [45] Yizhou Wang, Jen-Hao Cheng, Jui-Te Huang, Sheng-Yao Kuan, Qiqian Fu, Chiming Ni, Shengyu Hao, Gaoang Wang, Guanbin Xing, Hui Liu, et al. Vision meets mmwave radar: 3d object perception benchmark for autonomous driving. In *2024 IEEE Intelligent Vehicles Symposium (IV)*, pages 2769–2775. IEEE, 2024. 2
- [46] Zhongce Wang, Chao Jin, Lingzhang Sun, and Yunfan Li. Wrdi: A multimodal dataset of mmwave radar data and image. In *2021 IEEE International Conference on Big Data (Big Data)*, pages 3209–3214, 2021. 2
- [47] Sahil Waqar and Matthias Pätzold. A simulation-based framework for the design of human activity recognition systems using radar sensors. *IEEE Internet of Things Journal*, 2023. 2
- [48] Yingxiao Wu, Zhongmin Jiang, Haocheng Ni, Changlin Mao, Zhiyuan Zhou, Wenxiang Wang, and Jianping Han. mmhpe: Robust multi-scale 3d human pose estimation using a single mmwave radar. *IEEE Internet of Things Journal*, 2024. 2
- [49] Jianjian Yang, Tianmu Gui, Yibo Tong, Yuyuan Zhang, Qiankun Huang, and Guanghui Zhao. Autonomous mining transportation systems: Integrating 4d mmwave radar for enhanced detection of obstructed static objects. *IEEE Transactions on Intelligent Vehicles*, 2024. 2
- [50] Xiaotong Zhang, Zhenjiang Li, and Jin Zhang. Synthesized millimeter-waves for human motion sensing. In *Proceedings of the 20th ACM Conference on Embedded Networked Sensor Systems*, page 377–390, New York, NY, USA, 2023. Association for Computing Machinery. 2
- [51] Lianqing Zheng, Zhixiong Ma, Xichan Zhu, Bin Tan, Sen Li, Kai Long, Weiqi Sun, Sihan Chen, Lu Zhang, Mengyue Wan, Libo Huang, and Jie Bai. Tj4dradset: A 4d radar dataset for autonomous driving. In *2022 IEEE 25th International Conference on Intelligent Transportation Systems (ITSC)*, pages 493–498, 2022. 2

- [52] Junyu Zhou and Julien Le Kerneec. 4d radar simulator for human activity recognition. *IET Radar, Sonar & Navigation*, 2023. [2](#)